Eur. Phys. J. B **8**, 57–66 (1999)

THE EUROPEAN PHYSICAL JOURNAL B

EDP Sciences

Perylene hexafluoroantimonate: Suppression of the Peierls transition by anion-chain disorder

C. Buschhaus[1,2], R. Desquiotz[1], K. Eichhorn[2], M. Hofmann[1], K. Hümmer[2], V. Illich[1], M. Kelemen[1], S. Tarragona Auga[1], T. Wokrina[1], A. Zitsch[1], and E. Dormann[1,a]

[1] Physikalisches Institut, Universität Karlsruhe (TH), 76128 Karlsruhe, Germany
[2] Institut für Kristallographie, Universität Karlsruhe (TH), 76128 Karlsruhe, Germany

Received 17 July 1998

Abstract. Crystal growth and X-ray structural analysis are reported for the new quasi-one-dimensional organic conductor perylene hexafluoroantimonate. Due to deviation from exact 4:3 stoichiometry and anion-chain disorder the three-dimensional Peierls transition is suppressed to temperatures below 30 K in spite of a molecular field transition temperature of 330 K. Anisotropy of the microwave conductivity exceeds 3000:1 at room temperature. Curie paramagnetic defects with comparatively small electron spin resonance line width predominate at low temperature. Thermally activated paramagnetic defects, giving rise to pronounced Overhauser shift, are separated in the 30–100 K range. They are explained by neutral Perylene intra-stack defects, whose concentration can be reduced by both aging and annealing. The angular and temperature dependence of the conduction electron spin resonance line is analysed in detail, exhibiting the influence of intra-stack dipole interaction growing with temperature. Restricted diffusion of the conduction electron spins with diffusion coefficient of about 6 cm^2/s parallel to the stacking direction is detected by fixed gradient pulsed electron spin resonance at room temperature.

PACS. 61.65.+d Specific structure of organic compounds – 72.80.Le Organic semiconductors – 76.30.-v Electron paramagnetic resonance and relaxation

1 Introduction

The electrochemical crystallization of radical cation salts of simple arenes like fluoranthene (FA) or perylene (PE) with complex anions like hexafluorophosphate (PF_6^-) yields solids with various stoichiometries [1,2]. Such single crystals generally contain one-dimensional stacks of the flat aromatic hydrocarbon cations as structural characteristic [3] and exhibit quasi-one dimensional electrical conductivity [4]. Typically a Peierls transition to a low-temperature semiconductor phase with commensurate superstructure is observed in the 100 K to 200 K range [5,6]. Charge density wave (CDW) transport [7] and occurrence of two types of paramagnetic defects with or without pronounced electron spin resonance (ESR) line narrowing have been reported and analyzed [5,8] for the low-temperature phase. Recently we pointed to the fact that the three-dimensional Peierls transition seems generally to be preceeded by a structural phase transition related with anion ordering resulting in two-dimensional spatial correlation of the neighbouring one-dimensional stacks [9,10]. In this respect, characterization of a quasi-one dimensionally conducting radical cation salt with highly ordered arene stacks, but *disordered* anion chains is of especial interest, because the suppression of the three-dimensional Peierls transition would be expected. The realization of this goal is reported here.

Our report is organized as follows: growth of perylene hexafluoroantimonate from tetrahydrofurane solvent is described in Section 2.1. The crystal structure, analyzed by X-ray techniques (Sect. 2.2) is explained in Section 3.1 and indicates an approximate stoichiometry of $(PE)_4(SbF_6)_3$. Microwave conductivity, measured at different frequencies (Sect. 2.3), proves an anisotropy of the electrical transport of at least 3000:1 (Sect. 3.2). Sample aging as detected by ESR and microwave conductivity, is related to the loss of long-range correlations of the anion chains (Sect. 3.1.3). The detailed analysis of static and ESR magnetic susceptibility (Sects. 2.4 and 2.5) reveals two types of paramagnetic contributions, one of them thermally activated, in addition to Curie paramagnetic defects (Sect. 3.3). Our analysis indicates that anion disorder indeed prevents a 3D Peierls transition in these non-stoichiometric perylene hexafluoroantimonate salts.

[a] e-mail: edo@piobelix.physik.uni-karlsruhe.de

2 Experimental details

2.1 Crystal growth and elemental composition

Electrocrystallization of $(PE)_4(SbF_6)_{3-x}$ was performed by anodic oxidation in a three-compartment electrochemical cell at 15 °C using a saturated solution of zone refined perylene in tetrahydrofuran (350 mg PE and 1 g Bu_4NSbF_6 in 100 ml THF), platinum-foil electrodes and constant voltage (2.5–3 V). The needle like crystals with glossy surface were collected after two or three days. The general composition of the crystals was controlled by chemical elemental analysis. The mass distribution of 56.87% C, 2.86% H, 20.4% Sb, 16.4% F and 3.8% O corresponds to a composition $(PE)_4(SbF_6)_{3-x}$ with $x = 0.36 \pm 0.20$ ($PE = C_{20}H_{12}$). No indications for solvent inclusion were obtained. Sample aging in air at room temperature was accompanied by the glossy crystal surface turning into frosted appearence. Therefore single crystals were kept in a freezer at −18 °C when stored for extended period of time.

2.2 X-ray structural analysis

Small, black crystals – grown as described – were investigated with MoKα X-rays. Diffraction patterns were obtained using a MAR-Image-plate system. Data collection for structure solution and refinement was performed with a Picker-Stoe 4-circle diffractometer. The structure was solved and refined using the SHELX92 programs [11], scattering factors taken from [12], anomalous dispersion included, no absorption correction.

2.3 Microwave conductivity

The microwave conductivity σ was measured using the conventional cavity perturbation technique. At 10.2 GHz the reflection method and at 4.6 GHz, 9.3 GHz and 23.5 GHz a transmission set-up were used: at fixed temperature, the center frequency f_0 and the quality factor Q_0 of the empty cavity are determined. Then, the needle-like crystal sample is placed inside the cavity (typical sample size: diameter 0.16 mm, length 3.6 mm. For measurements of $\sigma_\parallel$, the needle axis is oriented parallel to the electric field). The center frequency f_p and the quality factor Q_p of the loaded cavity are measured. The sample is cooled by a gas flow cryosystem (He or N_2 gas). The experimental arrangement and the measurement performance are described in [13]. The frequency shift could also be analysed in order to determine the thermal expansion along the stacking direction – and needle axis – of high electrical conductivity.

2.4 Magnetic susceptibility

The static magnetic susceptibility was determined with a SQUID magnetometer (Quantum Design MPMS) for a large number of crystals at statistical orientation. During the measurements, the crystals were surrounded by a low pressure Helium atmosphere. The measured susceptibility is the superposition of four contributions

$$\chi_m = \chi_m^{Curie}(T) + \chi_m^{dia} + \chi_m^{ap}(T) + \chi^{ce}(T) \qquad (1)$$

i.e. the Curie like contribution of localized paramagnetic defects, χ^{Curie}, the molecular diamagnetism χ_m^{dia}, the thermally activated paramagnetism of neutral structural defects (described as singlet-triplet systems with activation energy ΔE_{ST}) and the temperature dependent conduction electron contribution $\chi^{ce}(T)$. The first two contributions could be determined and separated in the 5–35 K range, whereas the last two contributions could only be decomposed based on ESR analysis.

2.5 Electron spin resonance and Overhauser shift

Electron spin resonance and Overhauser shift were measured with a Bruker ESP 300 E spectrometer at X-band frequencies. We refer to [8] for experimental details. In addition, electron spin relaxation and diffusion was analyzed at room temperature and X-band frequency by pulsed ESR as described in [14].

3 Discussion of experimental results

3.1 Crystallographic structure

The X-ray diffraction patterns of $(PE)_4(SbF_6)_3$ show modulated diffuse lines of high intensity as well as sharp Bragg-reflections, indicating that perylene hexafluoroantimonate consists of both a well ordered and a severely disordered component. In a first attempt to solve the structure with direct methods the perylene molecules were found to form well ordered stacks while the anions seem to be completely disordered along chains running parallel to the perylene stacks. The crystallographic analysis will therefore be divided in two parts: solution of the average structure (Sect. 3.1.1) – only Bragg reflections are taken into account; characterization of anion-chain disorder (Sect. 3.1.2).

3.1.1 Average structure

The planar perylene molecules were easily found, but no stable refinement of any free set of atoms in the anion chains was possible. Therefore three independent (with respect to motion and rotation) and geometrically identical octahedra were refined on partially occupied sites. While the three Sb–F distances were refined freely the F–Sb–F angles had to be fixed at 90 degrees.

The perylene molecule arrangement corresponds to a Pmnn symmetry. Since an inversion center does not reduce the number of anion parameters and even does not prove to be necessary for modelling the anion chains, the space

Table 1. Crystal data and structure refinement.

Identification code	$(PE)_4(SbF_6)_3$
Empirical formula	C40 H24 F9 Sb1.50
Formula weight	858.22
Temperature	293(2) K
Wavelength	0.71073 Å
Crystal system	orthorhombic
Space group	P2*nn* (No. 34)
Unit cell dimensions	$a = 13.226(3)$ Å, $\alpha = 90°$
	$b = 14.184(3)$ Å, $\beta = 90°$
	$c = 4.1306(8)$ Å, $\gamma = 90°$
Volume, Z	774.9(3) Å^3, 1
Density (calculated)	1.839 Mg/m^3
Absorption coefficient	1.403 mm^{-1}
F(000)	422
Crystal size	$0.1 \times 0.08 \times 0.06$ mm
Theta range	2.87° to 20.01°
for data collection	
Limiting indices	$-12 \le h \le 12$,
	$-13 \le k \le 13$,
	$0 \le l \le 3$
Reflections collected	1389
Independent reflections	716 ($R(int) = 0.0228$)
	460 (with I $> 2\sigma$(I))
Refinement method	Full-matrix least-squares
	on F^2
Data/restraints/parameters	716/264/130
Goodness-of-fit on F^2	2.391
Final R indices ($I > 2\sigma(I)$)	$R1 = 0.0389, wR2 = 0.0749$
R indices (all data)	$R1 = 0.0801, wR2 = 0.0822$
Absolute structure parameter	0.1(3)
Largest diff. peak	$0.349e$ Å^{-3}
and hole	and $-0.315e$ Å^{-3}

Table 2. Atomic coordinates ($\times 10^4$) and equivalent isotropic displacement parameters (Å$^2 \times 10^3$). $U(eq)$ is defined as one third of the trace of the orthogonalized Uij tensor. The site occupation factors are Sb(1)–F(6): 0.1875, Sb(2)–F(18): 0.09375, C(1)–H(10): 1.0.

atom	x	y	z	$U(eq)$
Sb(1)	4999(5)	5046(2)	2146(6)	46(1)
F(1)	5627(9)	4167(7)	5436(21)	116(4)
F(2)	5904(8)	4609(6)	−1003(21)	116(4)
F(3)	4371(9)	5925(7)	−1144(22)	116(4)
F(4)	4095(8)	5483(6)	5294(23)	116(4)
F(5)	5898(9)	5967(7)	3286(23)	116(4)
F(6)	4100(9)	4125(7)	1005(23)	116(4)
Sb(2)	4993(5)	5109(3)	252(16)	19(1)
F(7)	5998(8)	5643(8)	3457(26)	52(4)
F(8)	5592(8)	5815(8)	−3062(25)	52(4)
F(9)	3988(9)	4575(8)	−2952(27)	52(4)
F(10)	4393(9)	4403(8)	3567(28)	52(4)
F(11)	4130(8)	6086(8)	1107(31)	52(4)
F(12)	5855(9)	4133(7)	−602(31)	52(4)
Sb(3)	5043(5)	5103(4)	4831(18)	30(1)
F(13)	4090(10)	4424(8)	7870(29)	47(4)
F(14)	3958(9)	5808(9)	3203(31)	47(4)
F(15)	5995(10)	5783(9)	1792(37)	47(4)
F(16)	6127(9)	4399(10)	6458(37)	47(4)
F(17)	5264(11)	6004(8)	7917(31)	47(4)
F(18)	4821(13)	4202(8)	1745(28)	47(4)
C(1)	934(5)	4590(2)	3959(8)	31(1)
C(2)	1831(5)	4175(3)	2868(10)	42(1)
C(3)	1825(5)	3396(3)	839(11)	50(1)
C(4)	929(5)	2998(2)	−109(8)	44(1)
C(5)	0	3388(3)	882(13)	33(2)
C(6)	0	4187(3)	2962(14)	32(1)
C(7)	−936(5)	4590(2)	3959(8)	31(1)
C(8)	−1832(5)	4175(3)	2868(10)	42(1)
C(9)	−1822(5)	3396(3)	839(11)	50(1)
C(10)	−932(5)	2998(2)	−109(8)	44(1)
H(2)	2447(5)	4428(3)	3519(10)	50
H(3)	2433(5)	3142(3)	118(11)	60
H(4)	935(5)	2466(2)	−1421(8)	52
H(8)	−2449(5)	4427(3)	3517(10)	50
H(9)	−2429(5)	3142(3)	117(11)	60
H(10)	−939(5)	2465(2)	−1421(8)	52

group chosen is P2*nn*. (The standard setting is P*n*2*n*, but for better comparison with PF_6 and AsF_6-salts c was chosen to be stacking direction.) To keep the total number of parameters as low as possible the perylene molecules were constrained to Pmnn symmetry. H-atoms were generated in ideal positions and refined with a riding model. Crystal data, results of structure refinement and atomic positions are listed in Tables 1 and 2.

The structure consists of two different but crystallographically equivalent types of perylene molecule stacks with perylene molecules inclined relative to the stacking axis in opposite directions. Stacks of the same type form rectangles in the a, b-plane, the center position being occupied by a stack of the second type (see Figs. 1 and 2). The short perylene molecule axis runs parallel to the a-direction, the long axis is inclined relative to the b-direction by an angle α_{PE} of $\pm 36.8°$ (the sign depends on the kind of stack). The distance perpendicular to the molecule plane of two neighbouring perylene molecules within one stack is $d_{PE} = 3.31$ Å. Table 3 gives relevant geometric results of the refinement.

3.1.2 Anion chain disorder

Linear disordered chains produce diffuse sheets with constant distance in reciprocal space [15]. Though every chain

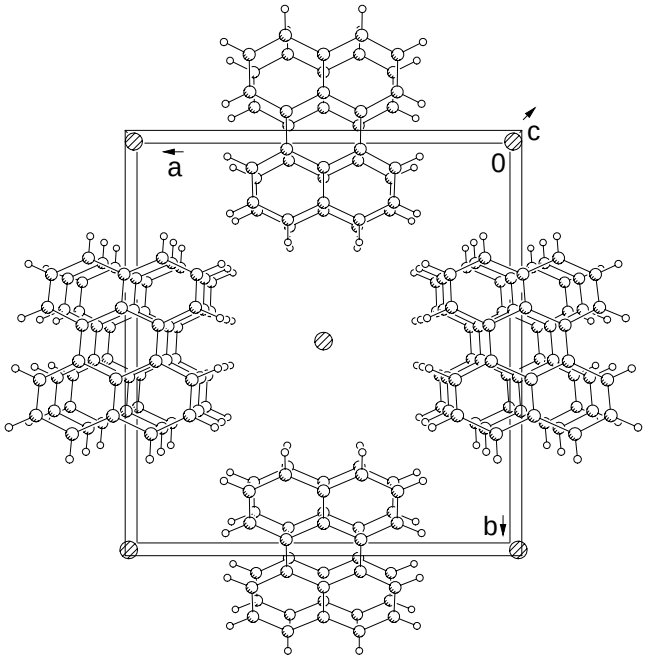

(a)

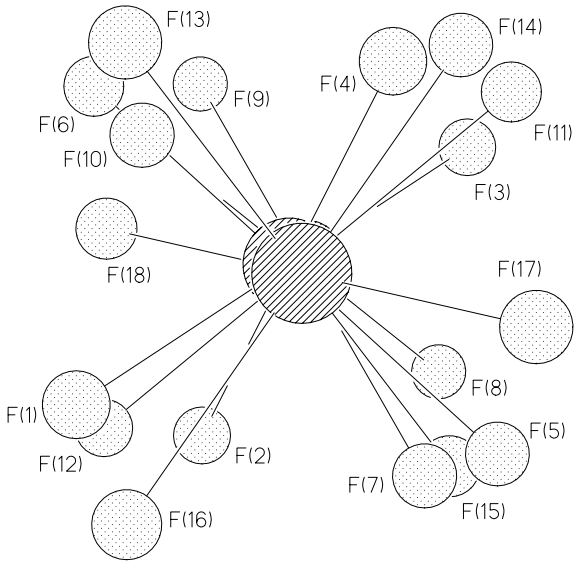

(b)

Fig. 1. (a) Structure of $(PE)_4(SbF_6)_3$, seen along c-direction, only PE molecules. (b) Orientation of the SbF_6-octahedra within the anion channels, seen along c-direction.

is well ordered, different chains are shifted against each other. There is no long range order perpendicular to the chain direction. Due to the heavy Sb atoms involved in the anion chain disorder this is clearly visible here in Figure 3. The ($l = 0$)-layer (projection of structure along the chain axis) is not diffuse. Therefore, different chains are only shifted against each other in chain direction. The inverse of the distance of the diffuse sheets can be interpreted directly as the Sb–Sb distance in the anion channel. Its value of $d_{\mathrm{Sb-Sb}} = 5.5$ Å is too large for a Sb–F–Sb

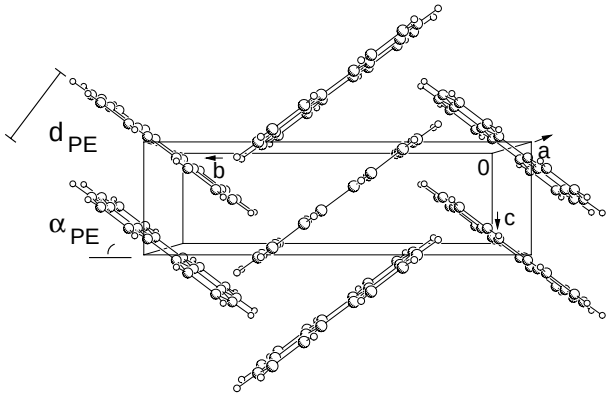

Fig. 2. Structure of $(PE)_4(SbF_6)_3$, seen along a-direction, only PE molecules.

Table 3. Geometric results of structure refinement Sb(2)–F(12) and Sb(3)–F(18) were constrained to be the same as Sb(1)–F(6).

d_{PE-PE}	3.31 Å
$d_{\mathrm{Naph-Naph}}$	1.445 Å
α_{PE}	36.8°
Sb(1)–F(5)	1.828(9) Å
Sb(1)–F(6)	1.829(9) Å
Sb(1)–F(2)	1.873(8) Å
Sb(1)–F(4)	1.873(8) Å
Sb(1)–F(1)	2.023(7) Å
Sb(1)–F(3)	2.023(7) Å

bridge. Thus, the occurrence of Sb_2F_{11}-molecules or even longer chains can be excluded.

The periodicity of the anion octahedra along the stacking direction is almost commensurate with the perylene structure. Every 4th diffuse layer falls together with every 3rd layer of Bragg reflections, giving a nominal perylene to SbF_6 ratio of 4:3. If perylene is considered to be built of two naphthalene molecules, their distance $d_{\mathrm{Naph-Naph}}$ is a measure of the average charge on the perylene molecule [17,16]. Here $d_{\mathrm{Naph-Naph}} = 1.445$ Å corresponds to an average charge of $q = +0.75e$ in accordance with the nominal perylene to SbF_6 ratio.

3.1.3 Sample aging

The intensity of the diffuse sheets is modulated. Figure 4 shows an intensity scan within the first diffuse layer, which can be fitted with Lorentzian line shapes not reaching the general background level between the intensity maxima. From the inverse of the half width at half maximum value one can estimate a correlation length of ~ 400 Å in both directions perpendicular to the chain axis.

The position of the intensity maxima points to a face centered orthorhombic "ideal"-crystal with a $2 \times 2 \times 4$ times enlarged unit cell. In fact, even fresh grown crystals show diffuse lines. If stored at room temperature

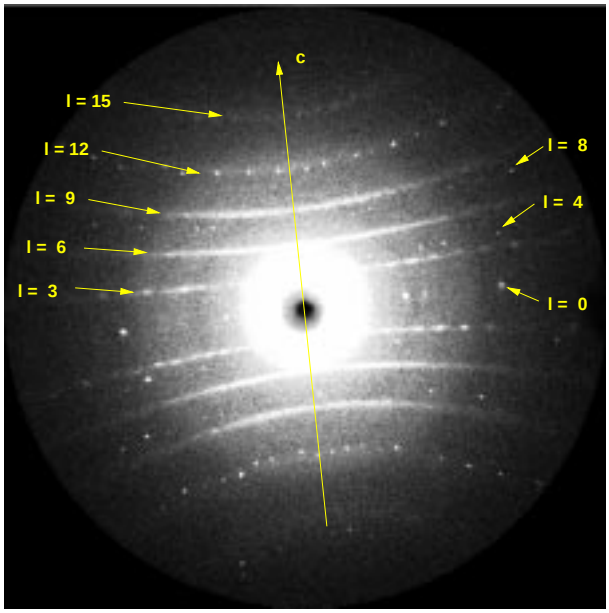

Fig. 3. X-ray diffraction pattern of $(PE)_4(SbF_6)_3$ shows diffuse lines and Bragg reflections.

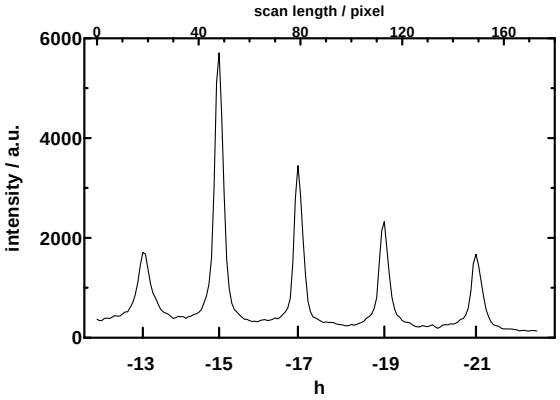

Fig. 4. Scan in a^*-direction within first diffuse layer $l = 3$ ($k = -7$).

the maximum intensities of the diffuse sheets drop until a constant diffuse background level is reached. This aging process indicates a further decrease of the correlation length perpendicular to the stacking direction.

3.2 Anisotropic microwave conductivity

Figure 5 shows the temperature dependence of the microwave conductivity σ at 10.2 GHz for electric field parallel and perpendicular to the stacking direction on a logarithmic σ scale. It resembles the variation of the CDW Peierls system diperylene hexafluorophosphate and arsenate [6], with the clear difference of the absence of any abrupt changes correlated with 3D-Peierls or other structural phase transitions. In the low-temperature range, an activation energy of about (14 ± 2) meV (and 15 meV for aged crystals) could be fitted. The anisotropy amounts to $\sigma_\parallel{:}\sigma_\perp \approx 3000{:}1$ at room temperature. It is thus larger

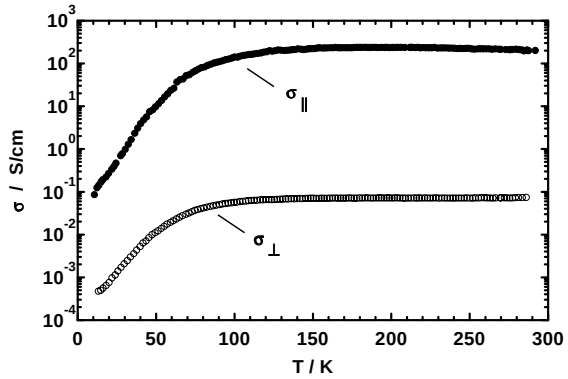

Fig. 5. Temperature dependence of microwave conductivity (10.2 GHz) parallel and perpendicular to PE-stacking axis in $(PE)_4(SbF_6)_3$ (logarithmic σ scale).

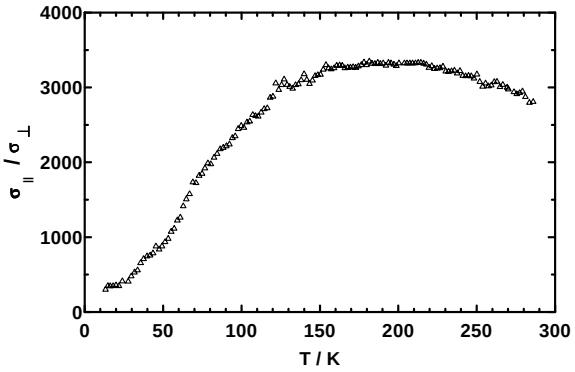

Fig. 6. Anisotropy of microwave conductivity in $(PE)_4(SbF_6)_3$ as function of temperature.

than the ratio observed for diperylene hexafluorophosphate and arsenate. As usually, $\sigma_\parallel/\sigma_\perp$ decreases with decreasing temperature (Fig. 6). The decrease is weaker and again without abrupt anomalies in contrast to the PE salts with 3D Peierls transition.

In order to visualize the high-temperature behavior more clearly, Figure 7 presents $\sigma_\parallel(T)$ and $\sigma_\perp(T)$ also on a linear scale. If an increase of the conductivity with lowering of the temperature is taken as a proof of "metallic" behavior, this conclusion is reached for transport parallel to the stacking axis and $T > 200$ K.

No frequency dependence of $\sigma_\parallel(T)$ was observed for 85 K $< T <$ 290 K, again at variance with the phosphate and arsenate salts. For the length scales probed at 4.6–23.5 GHz, the SbF_6-salts thus are "homogeneous" conductors due to a sufficiently large scale domain structure. A detailed theoretical analysis of the electrical conductivity is published elsewhere [18].

As a by-product, the microwave analysis showed that the expansion coefficient along the stacking axis amounts to $(65 \pm 6) \times 10^{-6}$ K^{-1} in the range 220 K $< T <$ 290 K and decreases for lower temperatures more than linearly. This large expansion must influence the conduction band width by reducing the π-electron overlap with increasing temperature.

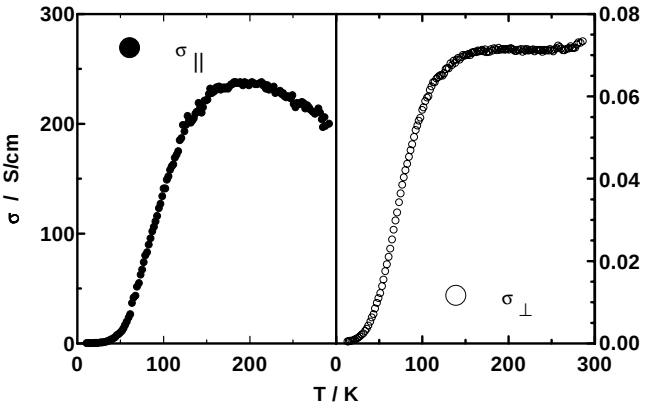

Fig. 7. Temperature dependence of microwave conductivity of $(PE)_4(SbF_6)_3$ for linear σ-scale, differentiating "metallic" $\sigma_{\|}$ and non-metallic $\sigma_{\perp}(T)$ high-temperature variation.

3.3 Static and dynamic magnetic properties

3.3.1 Curie paramagnetic localized defects

The separation of the magnetic susceptibility according to equation (1) indicated a concentration of Curie-like localized paramagnetic defects that varied with aging (within several months) from 3.8×10^{-2} to 6.5×10^{-2} spins $S = 1/2$ per formula unit for the large number (30–50 mg) of unselected crystals used for the SQUID measurements ($\chi_m^{dia} = (990 \pm 85) \times 10^{-6}$ emu/mole). The corresponding defect concentration of the small, selected crystals used for X-band ESR was clearly lower, amounting to about $(1.2 \pm 0.3) \times 10^{-2}$ spins $S = 1/2$ per formula unit $(PE)_4(SbF_6)_3$, only. This defect concentration is by two orders of magnitude larger than that in stoichiometric fluoranthene hexafluorophosphate salts [5] and by one order of magnitude larger than in the diperylene hexafluorophosphate salts whose disorder results primarily from built-in THF solvent molecules. Thus the influence of the deviation from exact 4:3 stoichiometry is evident.

We have earlier established that the g tensor of the PE radicals shows a clear anisotropy, with the g_{zz} factor for field perpendicular to the molecular plane being smallest and g_{yy} for field along the "short" PE in plane extension being largest [8]. Therefore the angular variation of the observed resonance positions was analysed, taking the inclination of the normal to the PE molecular plane by $\pm 37°$ with respect to the crystallographic c axis into account. (The ESR lines for the two alternating orientations were averaged and could thus not be distinguished by X-band ESR.) The anisotropy of the ESR line position of the Curie paramagnetic defects derived at 40 K did not differ from that of the conduction electrons characterized at 250 K (Tab. 4). Thus the Curie paramagnetic defects must be PE radicals built-in regularly in the perylene stacks, but probably linked to sites with deviations in the SbF_6 anion stoichiometry in the surrounding chains. Compared with other PE radical cation salts, the low-temperature ESR line width is rather small (increasing from about 0.08 G at 35 K to about 0.35 G at 10 K) thus revealing the delocalization of these defects that was compared with soliton like behavior for other radical cation salts [5,8].

Table 4. Calculated g-tensor of conduction electrons and thermally activated defects in $(PE)_4(SbF_6)_3$ at $T = 250$ K. z perpendicular to PE molecular plane; $x(y)$ in molecular plane, parallel to long (short) PE extension, as in [8].

	conduction electron	thermally activated defects
g_{xx}	2.00234(2)	2.00226(2)
g_{yy}	2.00300(2)	2.00299(2)
g_{zz}	2.00230(2)	2.00223(2)
$\bar{g}$	200255(5)	2.00249(5)

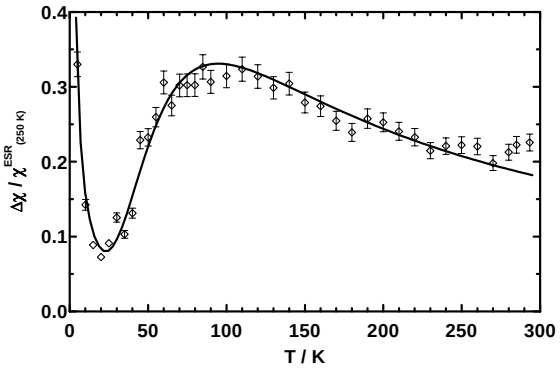

Fig. 8. Thermally activated paramagnetism of defects in $(PE)_4(SbF_6)_{3-x}$ normalized to total ESR susceptibility at 250 K. The solid line shows the fit of a Curie-like part and a singlet-triplet contribution with a triplet activation energy of $J/k_B = 157$ K.

3.3.2 Thermally activated paramagnetic moments

In the temperature range between 40 K and 200 K, the accurate description of the ESR lines required the superposition of two separate lines. One of them originates from the conduction electrons, the other one shows thermally activated behavior (Fig. 8). For simplicity, this temperature dependence was parameterized by the singlet-triplet model [19], see Figure 8, as was applied already for Di-naphthylethene-SbF_6 [20]. For aged crystals, *i.e.* 3 months later, this contribution's activation energy was reduced by almost a factor of two (from $J/k_B = 157$ K to 87 K, or $J = 13.5$ meV to 7.5 meV, respectively). In the same time, the respective concentration of initially $(1.3 \pm 0.3) \times 10^{-2}$ decreased by about 20%. It is interesting to note that the initial activation energy of the thermally activated paramagnetic moments and the low-temperature activation energy of microwave conductivity agree within the error bar. The ESR signal of these defects disappeared, if the crystals were annealed for one hour under nitrogen atmosphere at 333 K. These observations suggest that neutral PE molecules correlated with

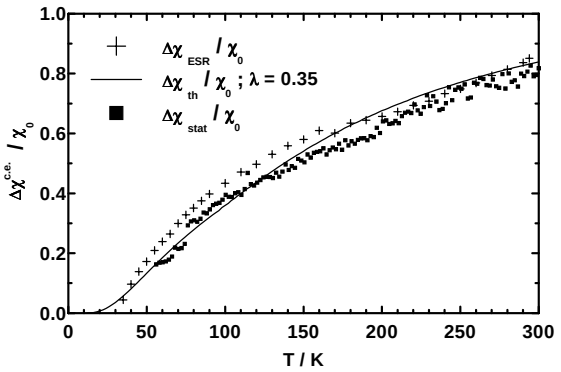

Fig. 9. Temperature dependence of conduction electron magnetic susceptibility of $(PE)_4(SbF_6)_3$. Experimental data from separation of static and ESR susceptibility (no separation of activated moments) are compared with model calculation for $T_{MF} = 330$ K. χ_0 (300 K) $= 297 \times 10^{-6}$ emu/mol is the bare (metallic) high temperature value [18].

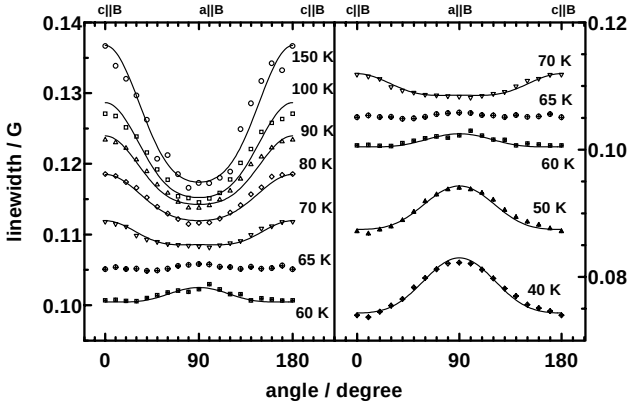

Fig. 10. Angular dependence of the conduction electron ESR line width of $(PE)_4(SbF_6)_3$ for magnetic field rotated in a, c plane starting from the stacking axis (c). The solid line shows the calculated variation explained in text.

substoichiometric composition in $(PE)_4(SbF_6)_{3-x}$ might be the source of the thermally activated paramagnetism. The g-anisotropy of the activated moments compares reasonably with that of the PE radical [8] or the conduction electrons (Tab. 4). The ESR linewidth is small, proving substantial exchange or motional narrowing of proton hyperfine and electron-spin dipole interaction: the linewidth increases from about 0.21 G at 65 K to about 0.26 G at 100 K, whereby the anisotropy decreases from about 0.02 G to 0.01 G. The anisotropy originates predominantly from proton hyperfine interaction as is revealed *e.g.* by the occurrence of a minimum for field parallel to the stacking axis [8]. Thus the thermally activated paramagnetic moments evidently do not form close, correlated intra-stack pairs.

3.3.3 Conduction electron ESR

The last contribution $\chi_m^{ce}(T)$ (Eq. (1)) decreases continuously with temperature as expected for a highly one-dimensional conductor (Fig. 9). The temperature dependence corresponds to the model prediction for a strictly one dimensional conductor, that shows no 3D-Peierls transition inspite of a comparatively high molecular field transition temperature $T_{MF} = 330$ K (resp. longitudinal electron-phonon coupling constant $\lambda = 0.35$ [18]).

The g anisotropy derived for the conduction electrons (Tab. 4) is temperature independent and in reasonable agreement with expectation for PE radicals (for inclination angle $\pm 37°$). It is by about 10% smaller than the anisotropy found for single-stack compounds earlier [8], however, indicative of some averaging by disorder.

The anisotropy of the linewidth of the conduction electron ESR line is presented in Figure 10. For temperatures above 80 K the angular variation of the linewidth could be reasonably described by the dipole-dipole interaction of intra-stack point dipoles in addition to an isotropic contribution (Eq. (4) in [8])

$$\Delta B = \Delta B_0 + 2d\tau \left(\frac{3}{8}(1 - 3\cos^2\theta)^2 + \frac{15}{4(1+(\omega\tau)^2)} \sin^2\theta \cos^2\theta + \frac{3}{8(1+(2\omega\tau)^2)} \sin^4\theta \right). \quad (2)$$

Line width and anisotropy increase with temperature for $T > 70$ K. This must be the influence of the growing portion of thermally activated defect spins. Their decreasing average separation influences the parameter "d" of equation (2) describing the dipole dipole interaction strength in [8]

$$d = \gamma_e^3 \hbar S(S+1)/r^6. \quad (3)$$

Similar behaviour was reported for the inorganic conductor $K_2Pt(CN)_4Br_{0.3}$ (KCP) by [21]. The linewidth of the *c.e.* ESR line decreases indeed during sample aging at room temperature. After annealing for one hour at 333 K, a width of the Lorentzian shaped *c.e.* line of only 55 mG at 250 K was observed, for reduced ESR line intensity, however. (As mentioned above, the signal of the activated spins disappeared as a consequence of this treatment.) In contrast to diperylene hexafluorophosphate [8], the product of dipolar field strength and correlation time "$d\tau$" in perylene hexafluoroantimonate is constant at high temperatures but decreases with temperature for T below 150 K (starting from about 1×10^{-2} G at 250 K), indicative of a weak temperature dependence of the correlation time ($\tau \approx 5 \times 10^{-12}$ s) [22]. In the low temperature range anisotropy of the hyperfine interaction with the PE protons is responsible for the linewidth anisotropy.

3.3.4 Local information via Overhauser shift analysis

The proton Overhauser shift, *i.e.* the shift of the ESR resonance condition due to the hyperfine interaction with

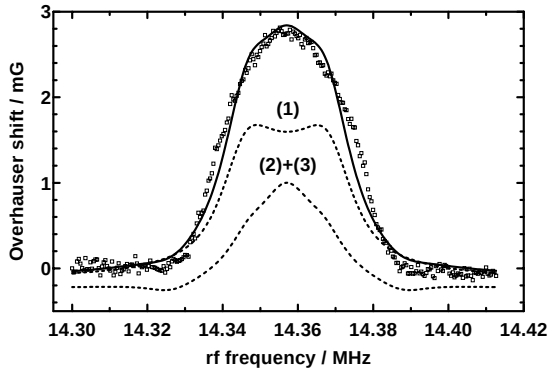

Fig. 11. Experimental and simulated proton Overhauser shift for magnetic field perpendicular to a axis at $T = 250$ K. (ESR saturation 85%, $rf - B_1 = 9$ mG, for further details see text; [23]).

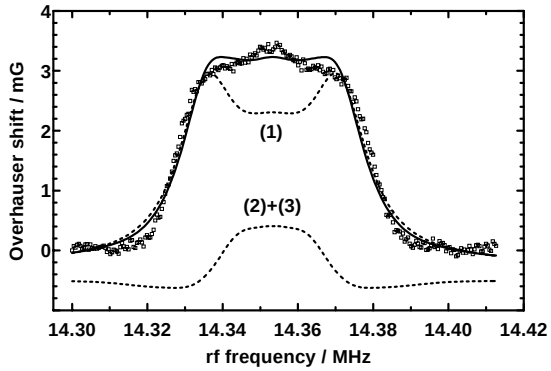

Fig. 12. Experimental and simulated proton Overhauser shift for magnetic field parallel to a axis at $T = 250$ K (ESR saturation 85%, $rf - B_1 = 9$ mG, for further details see text; [23]).

the dynamically polarized nuclear spins of the protons – was analyzed at ESR frequency $\nu_e = 9.45$ GHz, corresponding to a proton nuclear magnetic resonance frequency of about $\nu_{rf} = 14.3$ MHz [23]

$$\Delta B_{0v} = \frac{A}{g_e \mu_B}(1 + s\ V)\langle I_0 \rangle \qquad (4)$$

(with hyperfine coupling constant A, saturation factor $s \leq 1$, Overhauser enhancement V and thermal nuclear polarization $\langle I_0 \rangle$).

The results presented in Figures 11–13 were obtained for $P_e \approx 80$ mW, sufficient for 85% saturation of the ESR transition at 250 K. In spite of the weak thermal equilibrium value of the proton Overhauser shift of about 20 μG, the Overhauser enhancement factor $V(250\ \mathrm{K}) = 165$ allowed for easy detection of the enhanced Overhauser shift (Figs. 11 and 12). The spectrum of the Overhauser shift depends on the orientation of the crystal with respect to the magnetic field. The rf-spectral "position" reflects merely the intramolecular proton proton magnetic dipolar interactions, whereas the amplitude is dominated by hyperfine interaction, but influenced also by individual line width and transition probabilities in a complicated way.

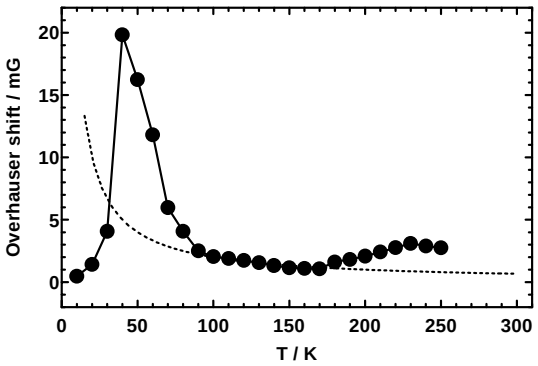

Fig. 13. Temperature dependence of the proton Overhauser shift. The broken line shows a $1/T$-law as is obeyed by the thermal proton nuclear spin polarization.

The numerical simulation included as broken and solid lines gives a reasonable but not unique description [23]. In addition to the total shift, given as solid line, the contribution of the four protons bound to carbons at position 1 (the inner positions at the short side of the PE molecule) and on positions 2 and 3 together (*i.e.* the two other proton carrying C sites) are given separately. For this simulation, the known anisotropy of the proton hyperfine interaction was used [24]. The local carbon spin densities $\rho_1 = 0.089 \pm 0.014$ and $\rho_2 + \rho_3 = -0.027 \pm 0.015$ were obtained from the fit. Generally in PE radicals, ρ_1 and ρ_3 are positive and ρ_2 negative, thus this result is not in conflict with this general trend.

Figure 13 shows an interesting result for the temperature dependence of the proton Overhauser shift. Evidently, the shift increases in the 40 K range much stronger than according to the Curie law of thermal proton spin polarization. In this temperature range, the thermally activated spins dominate the ESR signal, whereas the conduction electron susceptibility is reduced already drastically due to Peierls fluctuations. The Overhauser shift disappears, however, as expected at temperatures of 30 K and below, where the Curie-like defects predominate. This shows the action of motional and/or exchange narrowing for the ESR line of the activated spins, the well known prerequisite for Overhauser enhancement. We want to point to the similarity of the "peak" in Figures 8 and 13.

3.3.5 Conduction electron spin diffusion

The conduction electron spin – and presumably also charge – diffusion was analysed by pulsed ESR at X-band frequency. Figure 14 shows the dramatic anisotropy at room temperature. For magnetic field and gradient perpendicular to stacking axis, inspite of a magnetic field gradient of $G = 170$ G/cm, no deviation from the exponential T_2 decay is observed for the spin-echo attenuation. The corresponding decay constant of $T_2^* = 0.41$ μs compares reasonably with $T_2 = 0.39$ μs derived by direct T_2 measurement for field parallel to the stacking axis and the linewidth anisotropy presented in Figure 10.

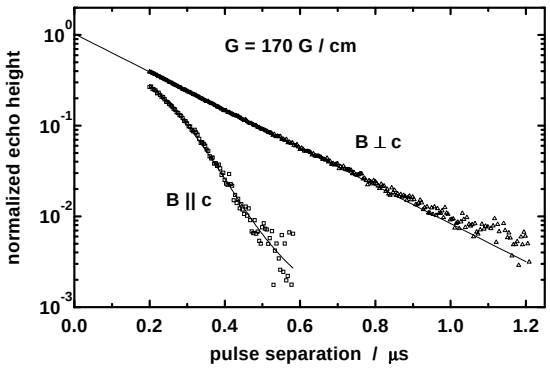

Fig. 14. ESR spin echo attenuation as a function of pulse separation for fixed gradient of $G = 170$ G/cm parallel or perpendicular to the stacking axis. The solid line fit is explained in text.

For magnetic field and gradient parallel to the stacking axis, the deviation from exponential decay is evident in Figure 14. The echo attenuation could be accurately described taking transversal spin relaxation with $T_2 = 0.40$ μs and restricted diffusion of the conduction-electron spins into account (Eqs. (13–16) of [14], Neuman and Robertson model)

$$E(2\tau) = E_0 \exp\left\{-2\tau/T_2 - \frac{8\gamma^2 G^2 l_s^4}{D\pi^6}\sum_{n=0}^{\infty}\frac{1}{(2n+1)^6} \times\left(2\tau - \frac{3 - 4e^{-Q\tau} + e^{-2Q\tau}}{Q}\right)\right\} \quad (5)$$

with

$$Q = D\frac{(2n+1)^2\pi^2}{\bar{l}_s{}^2} \quad (6)$$

and a chain length distribution

$$p(l_s) = \bar{l}_s^{-2} l_s \exp(-l_s/\bar{l}_s). \quad (7)$$

At 300 K a diffusion coefficient of $D = (6.3 \pm 0.2)$ cm^2/s and a characteristic stack length parameter of $\bar{l}_s = 97$ μm is obtained from the fit. The diffusion constant – or conduction electron scattering time – is thus clearly larger than values obtained in difluoroanthene or diperylene hexafluorophosphate or arsenate, whereas the characteristic diffusion length parameter $\bar{l}_s$ is surprisingly similar.

4 Conclusion

According to X-ray analysis, the PE molecules in perylene hexafluoroantimonate carry an average charge of $+0.75e$, indicating an intrinsic composition $(PE)_4^{3+\cdots}(SbF_6^-)_3$. Seo and Whangbo analyzed the electronic band structure with extended Hückel molecular orbital calculations. For $(PE)_4(SbF_6)_3$, *i.e.* $x = 0$, the conduction band of a full width of 0.6 eV would be 5/8 filled [16]. This corresponds to the band filling of diperylene hexafluorophosphate, if the extended band scheme is applied. The electronic properties of the PE-PF_6 radical cation salt required a description as $(PE)_4^{3+\cdots}(PE)_2^{\circ}(PF_6^-)_3 \cdot \frac{2}{3}$ THF (THF: built-in tetrahydrofuran solvent molecules), and the structural details (dimerization and tetramerization) indicated additional band splitting of the extended band into four subbands with the Fermi level in the middle of the third band for the "metallic" high temperature phase [8]. The tendency towards a Peierls distorted low temperature phase with periodicity of eight PE radicals (average charge $+0.75e$) could thus be expected – and seemingly observed – for $(PE)_4(SbF_6)_{3-x}$, $x \approx 0$ as well. Remember that the "ideal" orthorhombic room-temperature crystals cell contains four PE molecules in stacking direction (Sect. 3.1.3). Evidently the anion chain disorder prevents the three-dimensionally ordered Peierls-distorted low-temperature phase: down to the 35 K range, only the influence of the fluctuations announcing the Peierls transition are observed.

The relatively large value of $x \approx 0.36 \pm 0.20$ derived from elemental analysis points to the presence of a considerable portion of neutral PE molecules in PE-hexafluoroantimonate. Thus the existence of a distribution of shorter, 4:3-stoichiometric segments interrupted by anion-deficient regions with neutral PE molecules or singly charged PE dimers ($(PE)_2^{+\cdot}$, $q_{PE} = +0.5e$) must be expected. These defects explain the low-temperature paramagnetism reported above – the diamagnetic PE°-molecules are the source of the thermally activated paramagnetism, and the $(PE)_2^{+\cdot}$ centers may cause the Curie paramagnetism dominating at temperatures below 35 K. Within this frame, the aging behavior can be explained as well.

We are indebted to W. Brütting, H.W. Helberg, D. Schweitzer, and E. Weckert for discussions and H. Dragan, G. Mattern as well as I. Odenwald for experimental contributions. We thank Dr. P. Höfer and Bruker, Karlsruhe for the opportunity to perform the pulsed ESR measurements at 10 GHz. This work was financially supported by the Deutsche Forschungsgemeinschaft within the Sonderforschungsbereich 195 (Universität Karlsruhe). E. Dormann and T. Wokrina acknowledge a Grant from G.I.F., the German-Israeli Foundation for Scientific Research and Development.

References

1. Ch. Kröhnke, V. Enkelmann, G. Wegner, Angew. Chem. **92**, 941 (1980).
2. H. Endres, H.J. Keller, B. Müller, D. Schweitzer, Acta Crystallogr. C **41**, 607 (1985).
3. V. Enkelmann, K. Göckelmann, Ber. Bunsenges. Phys. Chem. **91**, 950 (1987).
4. Th. Schimmel, W. Rieß, G. Denninger, M. Schwoerer, Ber. Bunsenges. **91**, 901 (1987).
5. E. Dormann, G. Sachs, Ber. Bunsenges. Phys. Chem. **91**, 879 (1987).

6. M. Burggraf, H. Dragan, P. Gruner-Bauer, H.W. Helberg, W.F. Kuhs, G. Mattern, D. Müller, W. Wendl, A. Wolter, E. Dormann, Z. Phys. B **96**, 439 (1995).
7. W. Rieß, W. Brütting, Phys. Scripta T **49**, 721 (1993).
8. A. Wolter, U. Fasol, R. Jäppelt, E. Dormann, Phys. Rev. B **54**, 12272 (1996).
9. C. Buschhaus, E. Dormann, K. Eichhorn, K. Hümmer, R. Moret, S. Ravy, Z. Kristallogr. Suppl. No. **15**, 104 (1998).
10. V. Enkelmann, B.S. Morra, Ch. Kröhnke, G. Wegner, J. Heinze, Chem. Phys. **66**, 303 (1982).
11. G.M. Sheldrick, *SHELXTL. Version 5, Siemens Analytical X-ray Instruments Inc.* (Madison Wisconsin, USA, 1994).
12. *International Tables for X-Ray Crystallography*, Vol. C, edited by A.J.C. Wilson (Dordrecht: Kluwer Academic Publishers, 1992).
13. G. Schaumburg, H.W. Helberg, J. Phys. III France **4**, 917 (1994).
14. T. Wokrina, E. Dormann, N. Kaplan, Phys. Rev. B **54**, 10492 (1996).
15. A. Guinier, *X-Ray Diffraction* (W.H. Freeman, San Francisco & London, 1963).
16. D.-K. Seo, M. Whangbo (unpublished results).
17. G. Fischer, E. Dormann, Phys. Rev. B **58**, 7792 (1998).
18. R. Desquiotz, Ph.D. thesis, Universität Karlsruhe, Shaker Verlag Aachen, 1998.
19. O. Kahn, *Molecular Magnetism* (VCH Publishers Inc., 1993).
20. C. Raible, J. Gmeiner, H. Winter, E. Dormann, J.D. Stenger-Smith, V. Enkelmann, Synth. Metals **59**, 71 (1993).
21. T. Takahashi, H. Doi, H. Nagasawa, J. Phys. Soc. Jpn **48**, 423 (1980).
22. S. Tarragona-Auga, Diplomarbeit 1996, Universität Karlsruhe (unpublished).
23. V. Illich, Ph.D. thesis, Universität Karlsruhe, Shaker Verlag Aachen, 1998.
24. F. Hentsch, M. Hehnle, D. Köngeter, M. Mehring, Phys. Rev. B **37**, 7205 (1988).